1 Analysis of the technical biases of meteor video cameras
2 used in the CILBO system

3 **Thomas Albin[1], [2], Detlef Koschny[3], [4], Sirko Molau[5], Ralf Srama[1] and Björn**
4 **Poppe[2]**

5 (1) Institute of Space Systems, University of Stuttgart, Pfaffenwaldring 29, 70569 Stuttgart,
6 Germany

7 (2) Universitätssternwarte Oldenburg, Institute of Physics and Department of Medical Physics
8 and Acoustics, Carl von Ossietzky University, 26129 Oldenburg, Germany

9 (3) European Space Agency, ESA/ESTEC, Keplerlaan 1, 2201 AZ Noordwijk ZH,
10 Netherlands

11 (4) Chair of Astronautics, Technical Univ. Munich, Boltzmannstraße 15, 85748 Garching,
12 Germany

13 (5) International Meteor Organisation, Abenstalstr. 13b, 84072 Seysdorf, Germany

15 Correspondence to: T. Albin (albin@irs.uni-stuttgart.de)

1 Abstract

18 In this paper we analyze the technical biases of two intensified video cameras, ICC7 and
19 ICC9 of the double-station meteor camera system CILBO (Canary Island Long-Baseline
20 Observatory). This is done to thoroughly understand the effects of the camera systems on the
21 scientific data analysis. We expect a number of errors or biases that come from the system:
22 Instrumental errors, algorithmic errors, and statistical errors. We analyze different
23 observational properties, in particular the detected meteor magnitudes, apparent velocities,
24 estimated goodness-of-fit of the astrometric measurements w.r.t. a great circle, and the
25 distortion of the camera.

26 We find that due to a loss of sensitivity towards the edges, the cameras detect only about 55 %
27 of the meteors it could detect if it had a constant sensitivity. This detection efficiency is a
28 function of the apparent meteor velocity.

1   We analyze the optical distortion of the system and the 'goodness-of-fit' of individual meteor

2   position measurements relative to a fitted great circle. The astrometric error is dominated by

3   uncertainties in the measurement of the meteor attributed to blooming, distortion of the

4   meteor image, and the development of a wake for some meteors. The distortion of the camera

5   system can be neglected.

6   We compare the results of the two identical camera systems and find systematic differences.

7   For example, the peak magnitude distribution for ICC9 is shifted by about 0.2-0.4 mag

8   towards fainter magnitudes. This can be explained by the different pointing directions of the

9   cameras. Since both cameras monitor the same volume in the atmosphere roughly between the

10   two islands of Tenerife and La Palma, one camera (ICC7) is pointing towards the West, the

11   other one (ICC9) the East. In particular in the morning hours the Apex source is close to the

12   field-of-view of ICC9. Thus these meteors appear slower, increasing the dwell time on a pixel.

13   This is favorable for the detection of a meteor of a given magnitude.

2   Overview and scientific objectives

15   Recently, several multi-station video camera systems to observe meteors have been set up,

16   among others, in Japan (SonotaCo, et al. 2010, in Canada (Weryk et al. 2013) and in the US

17   (Cooke and Moser 2012, Jenniskens et al. 2011). The Canary Island Long-Baseline

18   Observatory CILBO is a double-station meteor camera setup operated by the Meteor Research

19   Group of the European Space Agency. It is part of the video camera system of the

20   International Meteor Organisation (Molau et al. 2015). CILBO consists of two stations, one

21   on Tenerife and one on La Palma. A small building with an automated roll-off roof houses a

22   set of video cameras with image intensifiers that monitor the same volume in the atmosphere

23   for meteors. The pointing of the cameras is such that their image centers point to a height of

24   100 km between the two islands. Analyzing the same meteor as seen from both camera

25   stations allows to derive the position relative to the Earth and, with that, to the cameras.

26   The main scientific goals of the setup are:

27   (a) To study physical and chemical properties of meteoroids, and, taking into account the

28   modifications of the meteoroid properties during their flight in the solar system, constrain the

29   physical and chemical properties of their parent body.

30   (b) To study the variability of the background dust flux in the Earth environment during a

31   complete year.

1   To fulfill these goals, the following measurements are needed: (a) flux densities of the
2   meteors, derived from the meteor numbers per time; (b) the physical properties of the
3   meteoroids, and their distribution, derived from light curves and velocity analysis; (c)
4   meteoroid orbits, derived from the double-station observations; (d) chemical properties of the
5   meteoroids, derived from spectra of the meteors.

6   A double-station setup is very well suited to address these points. Since the distances of the
7   meteor to the cameras can be determined, the absolute magnitude and the velocity in m/s can
8   be computed. From this, the mass of the underlying meteoroid can be estimated (see e.g.
9   Drolshagen *et al.* 2014, Ott *et al.* 2014, Kretschmer *et al.* 2015). This allows determining the
10   flux density of meteoroids as a function of mass. From the triangulation of the positions, the
11   3-d trajectory of the meteoroid in geocentric coordinates is determined. Together with the
12   velocity, the meteoroid path can be propagated backward and the heliocentric orbit of the
13   meteoroid can be determined. From the magnitude profile of the meteor some physical
14   properties of the object can be determined. To measure the spectra of the meteors, a second
15   camera is installed on Tenerife which has an objective grating.

16   To properly analyze all of these measurements, many biases have to be considered. Meteors
17   of a given mass will generate more light the higher their velocity when entering the
18   atmosphere. They will only be detected when they are above a certain brightness, which also
19   depends on the distance to the observing camera. Because of the optical effects of the camera,
20   they may be detectable in the center of the field of view but not at the edges, where the
21   camera sensitivity is lower. The higher the apparent velocity of a meteor, the more pixels are
22   covered per unit time by the meteor, making it more difficult to detect it. The observing
23   geometry will affect the observations - as we will show, a camera pointing to the east will
24   record more meteors than one pointing north. This is because the west-pointing camera sees
25   meteors from the Apex direction with lower apparent velocity, increasing the dwell time and
26   thus the meteors signal on a pixel.

27   In general we distinguish between two effects - geometrical and physical biases, and biases in
28   the detection system. This paper deals with the latter, the detection system, and with
29   geometrical aspects. The following section gives more background on the technical aspects of
30   the system. We first describe the setup and then summarize all the expected errors.

1   **3   Setup, data flow, and methods**

2   **3.1   CILBO overview**

3   A detailed overview of the setup is given in a previous paper (Koschny *et al.* 2013). In this

4   paper, we focus on the camera and the detection system, with an emphasis on their technical

5   performance. Figure 1 shows a photograph and a block diagram of one of the cameras. It

6   consists of the following main elements: (a) An objective lens type Fujinon, 25 mm f/0.8; an

7   image intensifier type DEP1700 with a fibre-coupled 2/3" CCD sensor read out via a Teli

8   CS8310BCi video camera. The resulting field of view is roughly 28° x 22° (H x V).

9   In the following, we are analyzing data from two cameras, called ICC7 (on Tenerife) and

10   ICC9 (on La Palma). 'ICC' stands for Intensified CCD Camera. Both cameras are identical.

11   They point to the same volume in the atmosphere, between the two islands. Thus their

12   pointing azimuth is roughly opposite; the pointing elevation is similar but not quite identical.
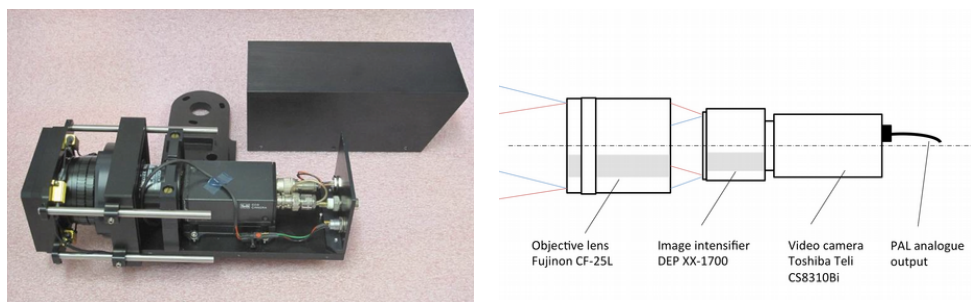
13   Figure 1: Photograph and sketch of the video cameras, called ICC (Intensified CCD Camera).

14   **3.2   Data flow**

15   The video cameras continuously record the night sky. With a field of view of approximately

16   600 deg^2, CILBO covers an area of around 3000 km^2 at an altitude of 100 km, where most

17   meteors appear. The camera delivers a PAL video stream via a professional frame grabber

18   card (Matrox Meteor II) to a Personal Computer. The video signal is searched in real time for

19   meteors using the software MetRec (Molau 1999). MetRec analyzes down-sampled images

20   with a resolution of 384 x 288 pixel^2 and 8 bit dynamical range. Later, we will show both full-

21   resolution data and down-sampled data, depending on the context.

22   MetRec generates a background noise image which is subtracted before the detection. The

23   detection algorithm itself is described in Molau (1999, 2014). The software searches for

1   brightness peaks in the background-subtracted images. It checks whether these peaks move on

2   a great circle from one frame to the next.

3   For each frame of a detection, MetRec records the total digital number of the event on the

4   detector and the position of its photometric center. For each detected event it stores a sum

5   image, an animation of the event, and a file containing detailed information on the event.

6   For each night, MetRec saves all files in a daily directory. The data for ICC7 and ICC9 are

7   stored in individual paths. The detailed information of each meteor is saved in an individual

8   ASCII file with the extension *.inf, henceforth called 'information file'. Additionally, MetRec

9   saves a log file that contains e.g. the used detection parameters, the used reference file which

10   contains the astrometric information of the stars and additional information of a recorded

11   meteor.

12   The complete content of an information file is, for each frame where the meteor was detected:

13   frame number, precise time taken from the computer clock, stellar magnitude of the event,

14   position of the photometric center in coordinates relative to the detector and in celestial

15   coordinates, and fitted coordinates as described in the following paragraph. An example

16   information file can be found in Koschny *et al.* (2013).

17   In addition to the information for each individual meteor, we use the log file entries in this

18   paper to characterize the system behavior. This file provides additional information for each

19   detected meteor.

20   The automated event detection runs every clear night, controlled by a scheduling software as

21   described in Koschny *et al.* (2013). At the end of the night, the data are uploaded to a central

22   server for further processing. On the next day, the data of each night is visually inspected and

23   false detections are deleted. The data are submitted on a monthly basis the video archive of

24   the International Meteor Observation, where a peer-review process ensures good data quality.

25   All data are available and searchable via the Virtual Meteor Observatory (Barentsen *et al.*

26   2008, http://vmo.imo.net).

27   MetRec allows to manually compare a grabbed image with a star chart to produce a so-called

28   'reference star' file. With this file MetRec can convert the relative positions together with the

29   time of the event to Right Ascension and Declination. The 'referencing' process also generates

30   a calibration file to convert pixel values to stellar magnitude. This process is typically done

31   only when the camera pointing has changed.

1   MetRec attempts to correct any measurement errors in the position determination. It takes the

2   originally measured Right Ascension and Declination values and fits them to a great circle.

3   The measured points are projected onto this great circle. In a next step, MetRec shifts the

4   points on this great circle to be equally spaced. For longer meteors (>7 frames), MetRec shifts

5   the points to match a distribution following a 2nd order polynomial.

6   If a second meteor appears during the same second as a previous on, an additional log entry

7   with the same time stamp is saved. However the corresponding information file with the

8   astrometric information is overwritten and lost.

9   **3.3   Expected errors**

10   3.3.1 Overview

11   In the later sections of this paper, we will present some findings on different parameters

12   measured by the system. Then we will draw conclusions on how important the different biases

13   are and which ones can be corrected. In summary, we expect the following errors.

14   3.3.2 Instrumental errors

15   (a) The mechanical / thermal instability of the mounting: Due to thermal effects, the precise

16   pointing position of the camera may change. This is a systematic error affecting the position

17   measurement of the meteor.

18   (b) The lens and possibly also the image intensifier generate a drop-off of the brightness

19   towards the edges of the field-of-view. This is a systematic error affecting the detectability of

20   a meteor.

21   (c) Due to the projection of the celestial sphere on the flat sensor surface, the system generates

22   distortion which needs to be corrected when computing positions of the meteors. This is

23   corrected by the 3rd-order polynomial 'plate fit' performed during the measurement, however

24   see Section 3.3.3 (c).

25   (d) The sensor is read out with 25 frames per second, the readout generates noise. In addition,

26   random noise is generated by the image intensifier. This noise can be quantified by obtaining

27   images with no light entering the system. It is a random noise affecting all measurements.

28   (e) The pixel resolution of the sensor does not match precisely the pixel format of the used

29   PAL format (768 x 586 pixels^2) and pixels may be interpolated.

1 (f) The sensor is an interline-transfer sensor, i.e. every second physical line on the sensor is

2 masked and used for readout. This and the previous point will reduce the quality of the

3 position determination of the meteor.

4 (g) (absolute) timing errors (offset of the computer clock): This is a systematic error that only

5 affects the position, not the velocity. A timing error of 1 s would correspond to a position error

6 in Right Ascension of 1/4' at the celestial equator.

7 (h) Distortion of the image of a meteor close to the edge of the field of view. This effect is

8 particularly pronounced for bright meteors and it will result in errors in the astrometric

9 position of the meteor.

3.3.3 Algorithmic errors

11 (a) Wake: During the movement of the meteor it may develop a train, which shifts the

12 photometric center to the opposite direction of the meteor's movement. This effect will result

13 in an apparent change in the velocity of the meteor. Typically, trains develop towards the end

14 of the meteor, so this effect will reduce the perceived speed of the meteor towards the end.

15 (b) Blooming: For bright meteors, so-called blooming may occur, i.e. electrons spill over from

16 one pixel to other adjacent pixels. The shift of the photometric center can then go in any

17 direction.

18 (c) The image distortion is corrected using a 3rd order polynomial fit. In particular towards

19 the edges of the field of view, a 3rd order may not be good enough to properly describe the

20 distortion. This will introduce a systematic deviation of the measured positions w.r.t. the real

21 position.

22 (d) When determining the position of a meteor, our detection software attempts to fit the

23 positions using a linear or quadratic equation for the apparent velocity. Due to geometric

24 effects this may not be sufficient to describe the position. This is a systematic error that affects

25 only the velocity. It is meteor dependent, as it is affected by the length of the meteor in

26 number of frames. The error may be estimated by calculating how the velocity will really

27 change when crossing the field of view, and how good the quadratic fit is. This will influence

28 the quality of the astrometric measurements.

29 (e) Meteor begin and end: Since the meteor will start or end at a random time during the

30 exposure of the first or last frame, taking the photometric center as the position of the meteor

1   for this frame is not giving correct results. This is a systematic error that only affects the

2   velocity.

3   (f) Quantization error of position in the information files: The position of a meteor is stored as

4   a relative position in the frame (from 0 to 1) with an accuracy of three decimal places only.

5   This corresponds roughly to 0.3 pixel. If meteor positions are recomputed later in the analysis

6   process this information is used, resulting a quantization of the position. This is a random

7   error which affects both position and velocity. It is meteor dependent, because meteors with

8   more frames will be less affected.

9   ### 3.3.4 Statistical errors

10 (a) Random scatter in the measurements: Both the position and the brightness measurements

11 of a meteor in an individual frame are affected. This is a random error due to the probabilistic

12 nature of the event. It affects both position and velocity and it can be derived from the

13 accuracy of the meteor fit you are currently investigating. It is meteor dependent, influenced

14 by the number of frames, meteor brightness, and possibly velocity.

15 In the following sections we characterize the camera systems in detail. We give results on

16 technical aspects related to camera and software (flat field effects, distortion...). We then

17 present statistics on overall distributions of different meteor characteristics (meteor length,

18 brightness...). We combine these results and provide, as a result, the means to properly debias

19 the data from the cameras for scientific analysis.

20 ## 4   Results

21 ### 4.1   Overview

22 Albin *et al.* (2015a, 2015b) have made a first attempt to analyze a selected number of bias

23 effects for meteors detected simultaneously with ICC7 and ICC9. Here we expand on this

24 work and also treat some of the data from the cameras separately. We use data from the

25 information and the log files.

26 The data flow followed the description in Section 2. We have used a total of 51062 and 56951

27 information files and 925 and 913 log files for ICC7 and ICC9, respectively. The analyzed

28 time range was from 13 Sep 2011 until 31 Aug 2015.

1   In the following sub-sections, we describe different parameters of the measurements. These

2   will be interpreted in the discussion section.

3   **4.2   Camera Sensitivity**

4   We start by analyzing the detection efficiency of both cameras vs. the apparent meteor

5   velocity in pixels per second. The detection efficiency is defined as the ratio of the

6   theoretically expected number of meteor detections on the CCD vs. the number of actual

7   meteor measurements on the CCD (Albin *et al.* 2015). Due to vignetting and projection

8   effects the cameras have a sensitivity drop to the edges and corners of the CCD. Thus, the

9   number of detections decreases to the edges due to the lower Signal-to-Noise Ratio (SNR) of

10   the meteor, which results in less detections by MetRec. In other words, the detection

11   efficiency would be 1 if a meteor of a given magnitude and velocity had the same SNR over

12   the complete field of view.

13   Figure 2 shows the flat field of the ICC7 system. The flat field of ICC9 looks similar. The

14   image is an 8 bit median stack of about 10 individual images, recorded when thin fog

15   provided a rather homogeneous sky background. The gray bar indicates the corresponding

16   normalized brightness. It can be seen that the intensity drops to the edges and corners of the

17   CCD. A lens with no vignetting or projection effects would lead to a uniformly shaped

18   distribution and a detection efficiency of 1. To compute the theoretically expected number of

19   measurements we take the part on the CCD with the highest detection density and extrapolate

20   this value for the complete CCD. A detailed description can be found in Albin *et al.* (2015a),

21   who also computed the detection efficiency for the CILBO system depending on the meteor

22   brightness. They found that the detection efficiency is at around 0.55 for meteors with a

23   brightness down to 4.5 mag and drops down to 0.45 and less for fainter meteors. This means

24   that the meteor cameras detect only half of the meteors which would be possible to detect for

25   an evenly illuminated sensor.
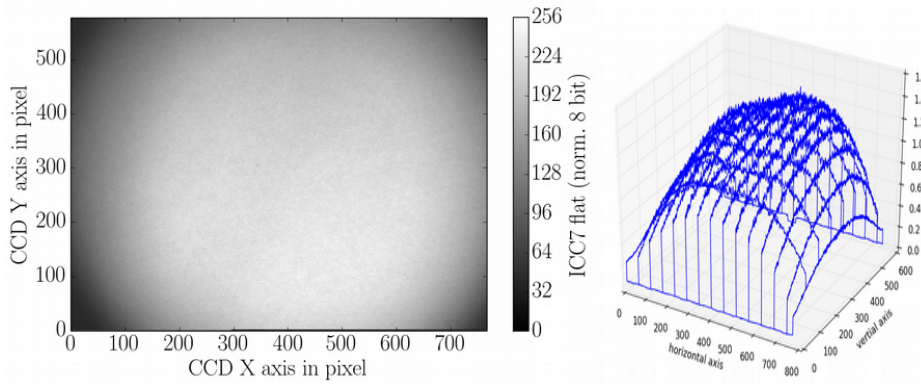
Figure 2 – 8 Bit median flat of the ICC7 camera. The X and Y axis are not down-sampled they cover the complete PAL signal. On the left, the image is shown, with the color bar indicating the brightness of the flat field. 256 is the maximum and can be found slightly off-centered to the right due to an offset in the optical system. The right panel shows a wire-mesh view of the flat field. Normalized values range from 0.3 in the corners to 1.3 in the middle.

Figure 3 shows the detection efficiency vs. the meteor velocity in pixels per second. For the analysis we use the filtered velocity data set from the information files. The data set has been divided into bins of 25 px/s. For each bin, the theoretical and actual number of meteor detections has been computed as in Albin *et al.* (2015a). The plot shows the detection efficiency from 0.0 px/s to 400 px/s. For very large velocities the number of data points decreases, increasing the shown standard deviation of the detection efficiency. It can be seen, that the detection efficiency is between 0.4 and 0.5 for meteors ranging from 0.0 px/s to 200 px/s. Then, the detection efficiency decreases approximately linearly for higher velocities.
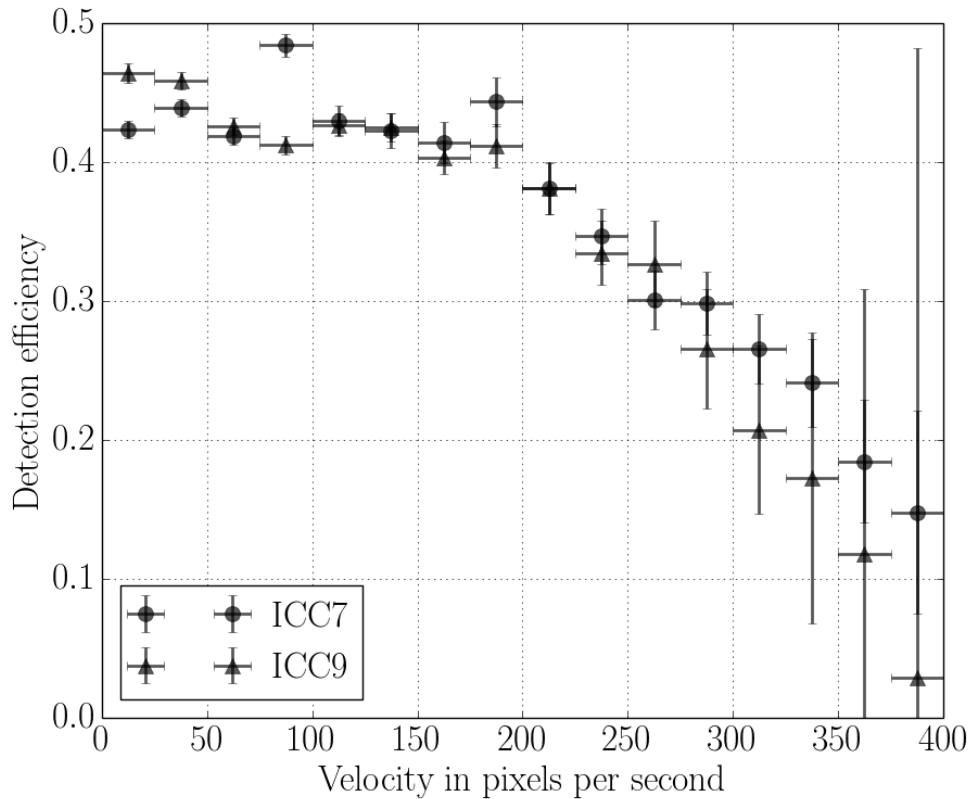
Figure 3 – Detection efficiency vs. the down-sampled velocity of a meteor in pixels per second. A detailed

description of the detection efficiency can be found in Albin *et al.* (2015a).

The pixel dwell time of a meteor is inverse proportional to the apparent meteor velocity on the CCD. Consequently, a higher meteor velocity decreases the SNR for a given meteor magnitude. The decreasing sensitivity to the edges and corners due to the projection effects result in a smaller effective detection area on the CCD for higher-velocity meteors. This can explain the lower detection efficiency for fast meteors.

The shown effects and the detection efficiency function as shown in Albin *et al.* (2015a) are necessary to de-bias the mass distribution of the meteors that is correlated to the brightness measurements. Additionally, the determined flux needs to be corrected by at least a factor of 2.

1   ### 4.3   Meteor velocity measurement bias

2   Albin *et al.* (2015b) described the velocity profiles of several simultaneously detected meteors

3   with the CILBO camera set-up. For the analysis they used the geocentric velocity in km/s

4   determined by the MOTS3 software package for computing trajectory data of double-station

5   meteor cameras (Koschny and Diaz 2002). Due to the atmospheric drag a meteoroid

6   decelerates during the atmospheric entry. We found that 40 % - 45 % of all meteors seem to

7   have an increased velocity between the first and second velocity measurement. This cannot be

8   explained by Earth's gravitational attraction. The effect is an observational bias of the camera

9   system. Both cameras are operated with a rate of 25 frames per second and a video frame

10   length of 40 ms respectively. The measurable beginning and ending time of a meteor does not

11   necessarily correspond to the video frame length of 40 ms. Consequently it may appear in the

12   dataset that the meteor covers a smaller distance at the beginning and end of a recording. The

13   ending part of the meteor overlaps additionally with the deceleration effect. Thus, to compute

14   a proper initial geocentric velocity from a continuously operated double station meteor

15   network the first and second video frame should not be used for the velocity computation. The

16   last velocity value should not be used for the same reason. As a result, no good velocity can

17   be determined for meteors recorded on 3 frames only. To obtain two velocity measurements,

18   the meteor has to be recorded on 5 frames.

19   ### 4.4   Accuracy values and optical distortion

20   We generated optical distortion maps to determine the astrometric deviations of the real star

21   positions relative to their expected positions according to the 3rd order polynomial plate fit

22   performed by MetRec. Figure 4 shows the computed distortion distribution for the ICC7

23   camera. The distortion is shown by plotting the deviation of the real measured star position

24   versus its expected position determined by the plate fit. It is given in arcminutes and is plotted

25   versus the radial distance from the CCD center in down-sampled pixels, The data are

26   summarized in bins of 10 pixels and visualized as a box plot[1]. It can be seen that the distortion

27   remains approximately constant until a radius of 140 pixels. The corresponding median is at

---

1   [1] A box plot is a way to visualize non-Gaussian distributions. It uses the so-called median and the inter-quartile

2   range (IQR). The median is the point where a distribution is divided into two equal-sized sets. The 25- and 75-

3   percentile are the lower and upper limit of the IQR; the IQR contains 50 % of the data around the median. In a

4   box plot, the median is shown as a horizontal solid line in a box; the box itself corresponds to the IQR. The

5   dashed line has a length of 1.5 IQR. Data points outside the IQR are plotted as crosses or grey circles.

1   around 0.1'. With the down-sampled horizontal image size of 388 pixels this corresponds to

2   80 % of the horizontal radius; 95 % of the horizontal radius are correct to 0.2'. Due to the

3   optical distortion of the lens, the values worsen to the corners up to 0.75'. In conclusion,

4   position measurements of meteors more than about 80 % away from the field center should be

5   used carefully.

6   Since the ICC9 distribution looks similar, only the ICC7 data are shown. We will see that

7   other astrometric errors are larger, and conclude that at least for the inner 90 % of the field of

8   view errors due to insufficient distortion correction can be neglected.
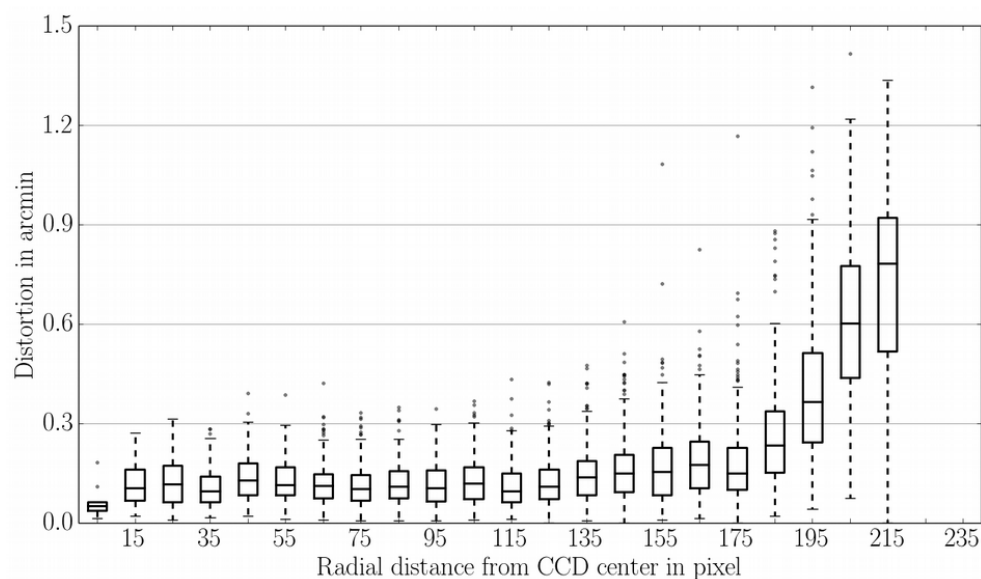
10 **Figure 4 – Boxplot of the ICC7 distortion. The difference between actual position and CCD position is**

11 **shown in arcminutes vs. the radial distance from the center of the CCD. Each box plot contains the data of**

12 **the a 10-pixel wide bin.**

13 ### 4.5   Measured astrometric goodness-of-fit

14 For each meteor, MetRec stores a value called 'accuracy' in the log file, which describes the

15 goodness of the fit of the individual meteor positions relative to a great circle in the sky. We

16 will henceforth refer to this as 'goodness-of-fit'. The value is given in arcminutes and is the

17 root-mean-square of the deviations of individual meteor position measurements to the

18 projections on a least-square great circle line. The smaller the value, the better the fit. This

19 section analyses the recorded accuracies.

1   Figure 5 shows the normalized goodness-of-fit distribution based on all meteor observations

2   for ICC7 (orange or bright bars) and ICC9 (blue or dark bars). 'Normalized' means that the

3   sum of all histogram bars is 1. The distribution plot is shown from 0.0' to 4.0' with a bin width

4   of 0.1'. This corresponds to the current accuracy resolution of MetRec. The maximum values

5   are around 10', but less than 3 % of the data are above 4' (2463 values out of 73379). We

6   therefore decided to not display them.

7   It can be seen that both cameras detect a significant number of meteors with a goodness-of-fit

8   of 0.0'. Values of 0.1' and 0.2' are missing completely. The log files show that ICC7 has 3899

9   (approximately 8 %) and ICC9 has 6527 (approximately 11 %) of all measurements with

10   values of 0. For both cameras, around 55 % of all measurements correspond to meteors with a

11   length of 3 frames. Around 20 % correspond to a length of 4 frames, 10 % and 5 % to 5 and 6

12   frames, respectively. The remaining 10 % correspond to longer meteors. A fraction of these

13   can be explained with the fact that MetRec rounds the determined goodness-of-fit. However,

14   most data points in this bin seem to have been falsely generated, otherwise the gap between

15   the 0.0' bin and next bin at 0.3' cannot be explained. The following accuracy-related analysis

16   therefore neglects these data points.

17   The median and interquartile range (IQR) of the ICC7 and ICC9 accuracies are

18    $ICC7_{acc} = 1.2^{+0.9}_{-0.5}$ ' and $ICC9_{acc} = 1.0^{+0.5}_{-0.3}$ '.
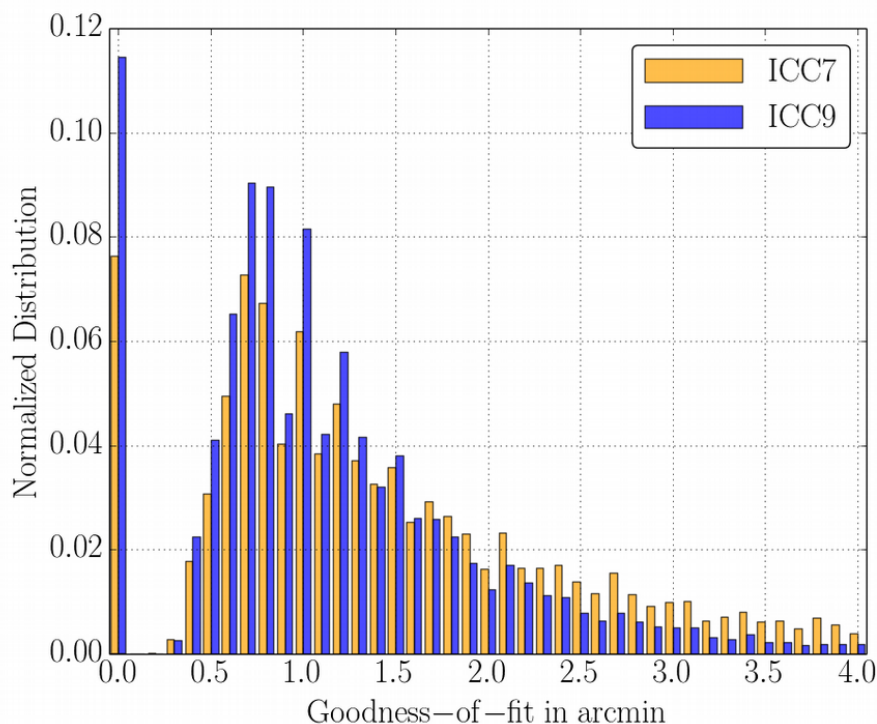
Figure 5 - Normalized distribution of determined goodness-of-fit in arcminutes. The orange and blue bars show the distribution for ICC7 and ICC9, respectively. The bars are slightly off-centered and have an actual width of 0.1', e.g.: the first two bins show the contribution of [0.0', 0.1') for ICC7 and ICC9.

5   MetRec uses half resolution images for the detection, *i.e.* 288 x 384 pixel^2. The obtained

6   average goodness-of-fit is thus about 1/4 pixel. For telescopic position measurements better

7   accuracies (up to 1/10 pixel) can be achieved. However, taking into account that the used

8   sensor is an interline transfer video chip and the field of view is rather large, this result is

9   acceptable.

10   When using these data to compute orbits, one can use the goodness-of-fit values to estimate,

11   via Monte-Carlo runs, the errors of the orbital elements. To simplify this preocedure, it is

12   proposed to use an average error value as derived in the following.

13   Figure 6 shows a box plot of the complete accuracy data of ICC7 and ICC9 in arcminutes

14   versus the length of a meteor measured in number of frames. All goodness-of-fit values from

15   the log files have been used with the exception of the 0.0' data. The Figure shows the

1   distribution between frame 3 and 40 and the number above each box gives the number of data

2   points in the corresponding bin. The longest meteor recorded with CILBO is about 80 frames.

3   For a better visualization and readability we show only data until 40 frames. For higher

4   values, the total number of measurements drops further and does not allow any statistical

5   conclusions. It can be seen that the median, the IQR, and 1.5·IQR range increase for meteor

6   lengths of 3 to 7 frames. The median increases from 1.1' to around 1.5'. From 7 to 8 frames,

7   the accuracy jumps to better values: The median drops to 1.0'. This is due to a setting in the

8   MetRec fitting algorithm. Up to 7 frames, the program uses a linear velocity function to fit the

9   meteor data. A meteor which is recorded on 8 or more frames is fitted with a quadratic fit

10   which leads to a better goodness-of-fit, as can be seen in the changing box size between frame

11   7 and 8. For meteors of length 8 to 40 frames, the accuracy worsens again slightly. The

12   number of data points which lie outside the box plots decreases for higher frame numbers.

13   The largest data scatter can be seen for meteor recorded on 3 frames. In some cases the

14   goodness-of-fit becomes as bad as 10'.
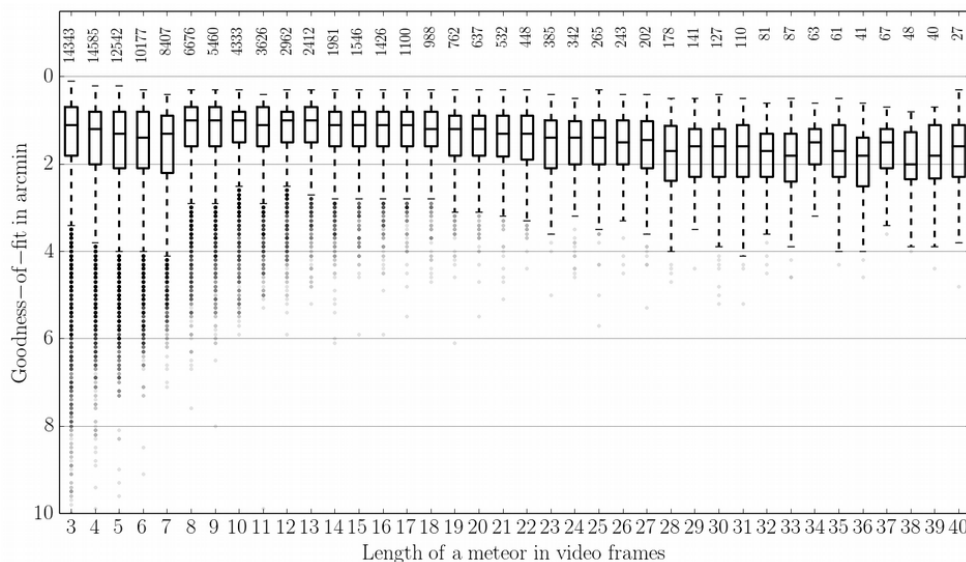
Figure 6 – Goodness-of-fit vs. frame length. The box plots show the median, Inter-Quartile Range (IQR)

and 1.5·IQR. The numbers on the top show the number of data points for each bin.

18   In conclusion, we suggest to assume a typical deviation of about 1.0'-1.2' to cover all

19   uncertainties in the astrometry. This corresponds to about 1 pixel.

4.6 Magnitude Distribution

ICC7 and ICC9 have the same technical setup and are operated in a similar way. Items like the detection threshold and the minimum number of frames per meteor are identical. Here, we compare the measured brightness distribution of both CILBO cameras, to check whether deviations in the data can be identified. For our analysis we assume that meteors appear randomly on the sky. Since some meteors either begin or end outside CILBO's field-of-view (FOV) or both, we consider only meteors which were completely within the FOV. Otherwise a bias or offset in the meteors' brightness profile would affect the statistics. For the analysis we take only meteors into account that are not closer to the CCD edges than 5 % of the length and width of the CCD, respectively. Thus, the data set reduces to 49494 meteors for ICC7 and 54402 meteors for ICC9 which corresponds to 97 % and 96 % of each individual data set, respectively.

Figure 7 shows the normalized distribution of the ICC7 and ICC9 brightness data vs. the peak brightness values in magnitudes. The orange (brighter) curve corresponds to the ICC7 data and the blue (darker) curve corresponds to the ICC9 data. The median and corresponding IQR for both cameras are $ICC7_{mag,peak} = 2.92^{+0.76}_{-0.97}$ mag and $ICC9_{mag,peak} = 3.32^{+0.70}_{-0.88}$ mag, respectively. This shows that ICC9 detects fainter meteors than ICC7. The brightness median difference between both cameras is 0.40 mag. We will show later that this is due to the different pointing directions of the cameras. Thus, the pointing affects the detected number of meteors for a given magnitude.
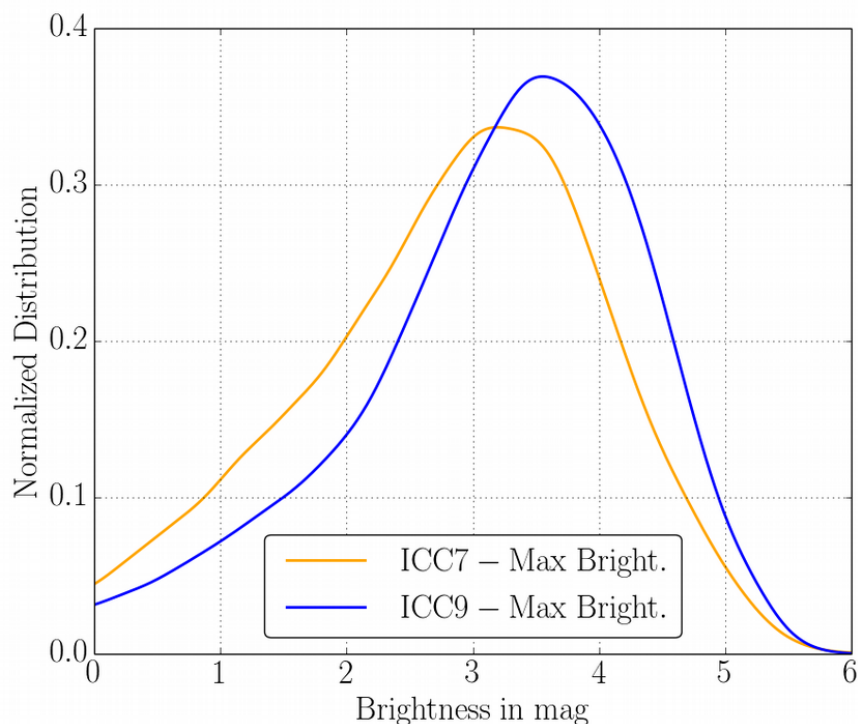
Figure 7: Normalized distribution of the peak brightness in magnitudes. The orange and blue curve correspond to the ICC7 and ICC9 camera, respectively.

4.7 Distribution of the length of a meteor in frames

MetRec's detection threshold is currently set to 3 frames. With 25 frames per second this corresponds to a meteor duration of larger than 40 ms (starting at the very end of the exposure of the first frame, ending at the very beginning of the last one) to 120 ms. In some rare cases a meteor with 3 frames can also have an appearance time of e.g. 160 ms, due to frame drops in the detection pipeline.

Figure 8 shows the normalized distribution of the length of the meteors in number of frames. The solid histogram represents the ICC7 data and the dashed histogram shows the ICC9 data. CILBO detects meteors with a length of up to $70 - 80$ frames. For a better data readability we show here the distributions up to a length of 15 frames, corresponding to a meteor appearance time of 0.6 seconds. It can be seen that the number of meteor recordings decreases for longer events. Both distributions peak at meteors with a length of 3 frames. For increasing lengths,

1   the number of meteors decreases faster for ICC9 than for ICC7. ICC7 detects more meteors

2   on 3 to 7 frames than ICC9. Afterwards, the ICC7 distribution is slightly above the one of

3   ICC9.
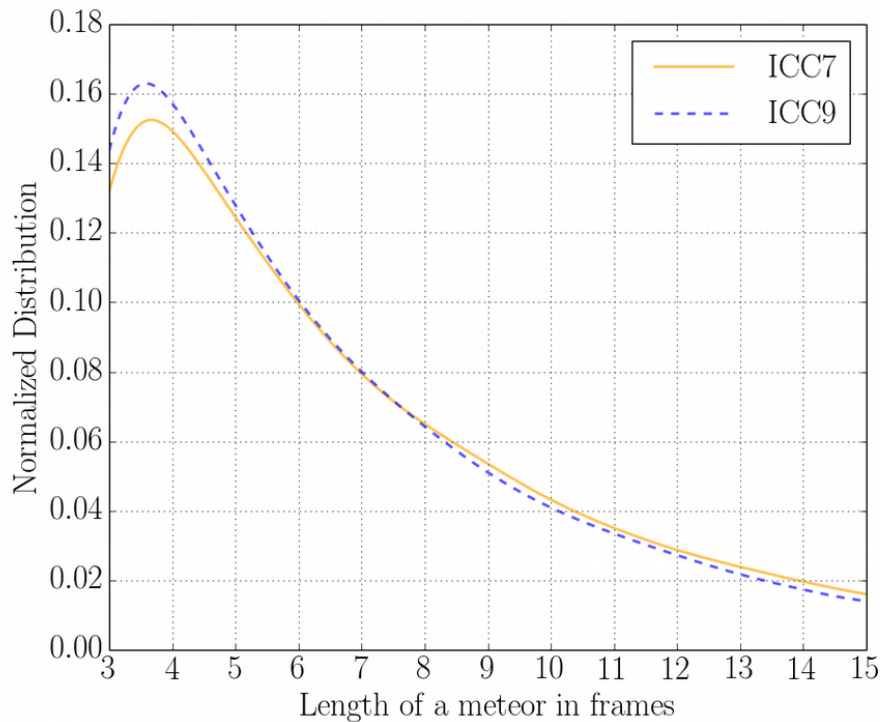
5   **Figure 8: Normalized distribution of the recorded frames for ICC7 (solid curve) and ICC9 (dashed curve).**

6   **Since MetRec's detection threshold is set to 3 frames, no meteors are recorded on fewer frames.**

7   ## 4.8 Velocity distribution

8   The apparent velocity of a meteor is computed from its position in each frame and assuming

9   that the frame rate is 40 ms. The position of a meteor is available in two coordinate systems:

10 Firstly, in a CCD-fixed system given as x/y value pairs, corresponding to the horizontal and

11 vertical position on the sensor, counted from the lower-left corner. x and y are normalized and

12 range from 0 to 1. To convert the positions in pixels, x and y need to be multiplied by a factor

13 of 768 and 576, respectively, which corresponds to the PAL resolution. Since MetRec

14 downsamples both axes by a factor of two we use values of 384 x 288 pixels^2 for all

15 detection-related aspects in this paper.

1   The second coordinate system which MetRec provides the astrometry in is the equatorial

2   coordinate system, where the meteor position is given in Right Ascension and Declination.

3   Due to optical distortions, the angular velocity distribution in degrees differs from the

4   distribution given in CCD coordinates depending on the position in the field of view. Since

5   this paper focuses on the technical aspects of the CILBO cameras, we consider in the

6   following only the apparent velocity in the CCD-fixed coordinate system. For those who

7   prefer to think in degrees per second, note that 100 px/s will be roughly 7 deg/s with the field

8   size of our cameras.

9   Figure 9 shows the density distribution of ICC7 and ICC9 versus the velocity in pixels per

10   second. The solid curves are the distributions of all mean meteor velocities, where the orange

11   (lighter) curve corresponds to ICC7 and the blue (darker) curve corresponds to ICC9 data.

12   The velocity axis ranges from 0 to 300 px/s (about 21 deg/s). It can be seen that both

13   distributions have a similar shape, however ICC9 converges faster to 0 than the ICC7

14   distribution. This means that ICC7 records more fast meteors than ICC9. The curve for ICC7

15   is flatter and crosses that for ICC9 at 195 px/s. The median and IQR (given as the error

16   values) for ICC7 and ICC9 are $ICC7_{vel} = 158^{+151}_{-77}$ px/s and $ICC9_{vel} = 146^{+93}_{-66}$ px/s,

17   respectively. This shows quantitatively that the ICC7 distribution is wider spread.

18   Meteors appear and disappear at some arbitrary time during the exposure time of the first and

19   last frame of a detection (see Section 4.4). Thus, normally the determined photometric centers

20   of the first and last frame are shifted towards the photometric centers determined from the

21   second and second-to-last video frame, respectively. To compute the velocity, the time

22   interval between two frames is used, namely 40 ms. This means that the first and last velocity

23   determination typically are under-estimated. We leave away those values and call this the

24   filtered velocity data. The dashed curves in Figure 9 show the filtered mean velocity data sets

25   of ICC7 and ICC9. Both dashed curves appear similar to the solid ones. The median and IQR

26   values for both filtered datasets are $ICC7_{vel,unbiased} = 157^{+149}_{-76}$ px/s and

27   $ICC9_{vel,unbiased} = 150^{+95}_{-67}$ px/s, corresponding to roughly 10 deg/s.

28   In the following sections we only use the filtered velocity data set if not otherwise mentioned.

29   We suggest velocities computed from the first and last recorded frame should not be used.
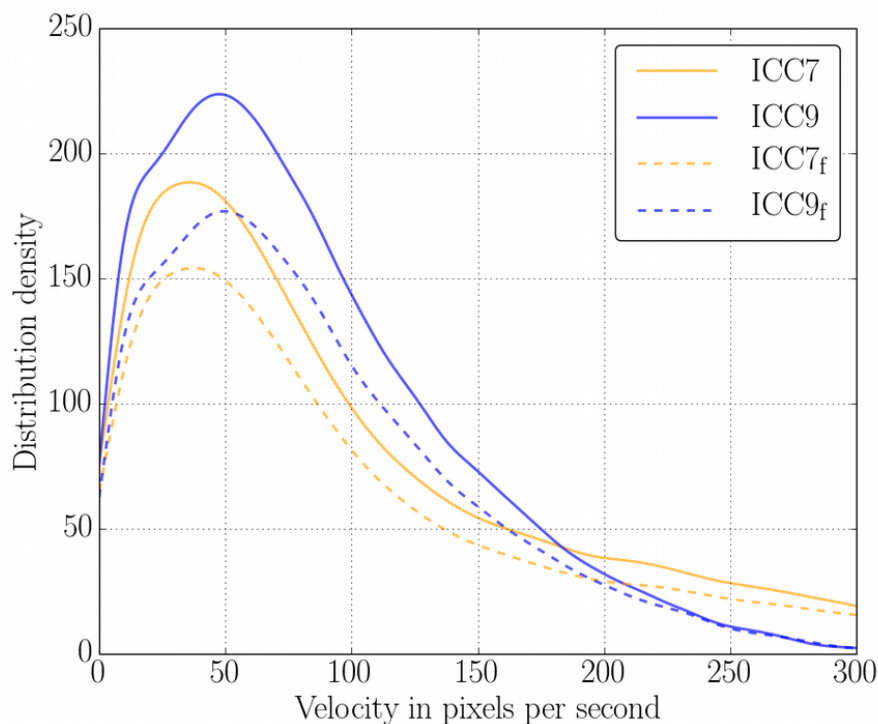
Figure 9 - Distribution of the meteor velocities in pixel per second. The orange (bright) curves correspond to ICC7 and the blue (dark) curves show the ICC9 data. The solid distributions show the complete data set, containing all determined velocities. The dashed curves show the filtered velocity data set as explained in the text.

4.9   Correlation between different measurements

4.9.1 Overview

In Sections 4.2 to 4.8 we showed distributions of different measured values like the accuracy or brightness of a meteor as determined by MetRec. Both ICC cameras are identical, but show deviations in the measured parameters. This section investigates possible correlations between certain measurements and parameters.

First, we describe the dependencies between the measurements and the recorded frame length. Afterwards we investigate possible detection time correlations. The last two sub-sections show some correlations with the measured brightness and determined velocities.

1   ### 4.9.2 Peak magnitude as function of meteor length and velocity

2   Figure 10 to Figure 13 show box plots of the maximum brightness of a meteor in magnitudes

3   and filtered mean apparent velocity in pixels per second for ICC7 and ICC9, respectively. The

4   data are plotted vs. the length of a meteor in frames. Only meteors which were detected

5   completely within the FOV of the cameras are considered.

6   The median and corresponding IQR of the brightness data for ICC7 and ICC9 show that the

7   maximum brightness increases for longer meteors. Meteors with a length of 3 frames have a

8   median and IQR of $3.4^{+0.6}_{-0.6}$ mag for ICC7 and $3.8^{+0.6}_{-0.5}$ mag for ICC9. It can also be seen

9   that the medians and IQRs of ICC9 are shifted towards fainter meteors by a factor of around

10   0.2 - 0.4 mag, consistent with Figure 7.

11   The box plots of the velocity distributions for ICC7 and ICC9 (Figure 12, Figure 13) show a

12   slight difference. Median and IQR for ICC9 are basically constant for all shown meteor

13   lengths. The IQR ranges between 50 and 150 px/s. ICC7, however, shows a decrease in the

14   velocity for an increasing number of video frames. The maximum is at the beginning where

15   the median is at around 75 px/s and the IQR boundaries are at 40 px/s and 140 px/s. The

16   decreasing median and IQRs converge with the ICC9 data at around frame 11.
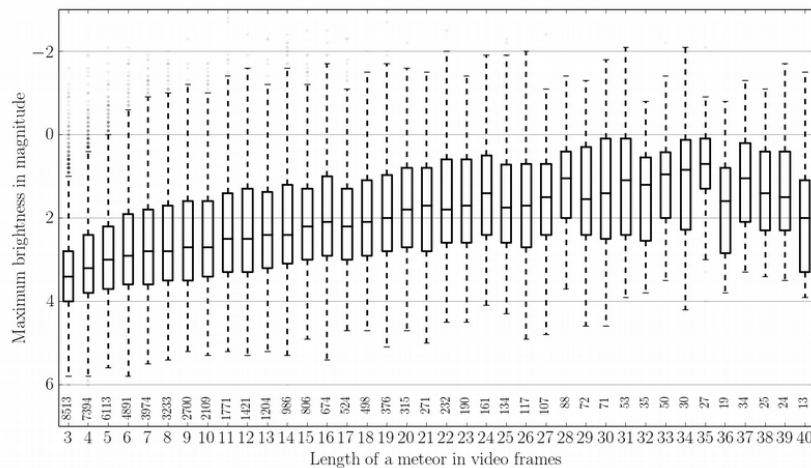
18   **Figure 10 - Maximum brightness in magnitude vs the length of the meteor in frame numbers for ICC7.**

19   **The box plot shows the median, IQR and 1.5·IQR. The number shown on the bottom indicates the number**

20   **of used data points per frame bin.**
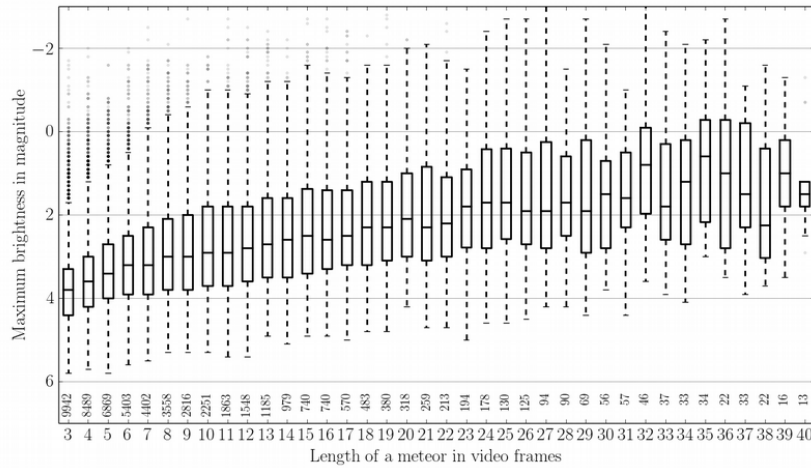
Figure 11 - Maximum brightness in magnitude vs length of the meteor in frame numbers for ICC9. The box plot shows the median, IQR and 1.5·IQR. The number shown on the bottom indicates the number of used data points per frame bin
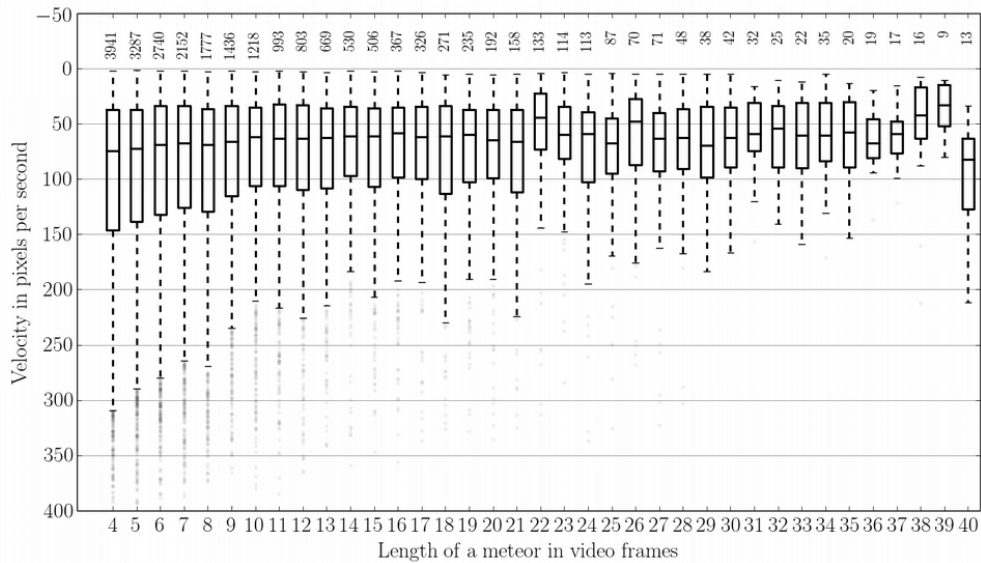
Figure 12 - Apparent meteor velocity in pixels per second versus the video frame length for ICC7. The box plot shows the median, IQR and 1.5·IQR. The number shown on the top indicates the number of used data points per bin.
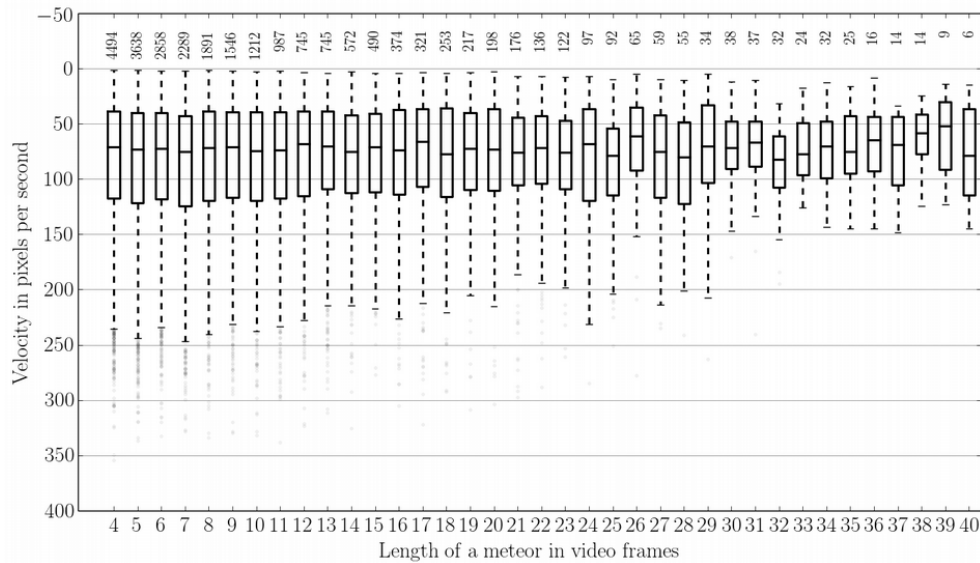
Figure 13 - Apparent meteor velocity in pixels per second vs the video frame length for ICC9. The box plot

shows the median, IQR and 1.5·IQR. The number shown on the top indicates the number of used data

points per bin.

4.9.3 Goodness-of-fit versus peak magnitude

Figure 14 and Figure 15 show the measured goodness-of-fit versus the average peak

brightness in mag for ICC7 and ICC9, respectively. We use all goodness-of-fit values larger

than 0.0'. The shown figures show the data up to 6.0' in a magnitude range from -2.0 mag to

6.0 mag. The solid line, box and the dashed lines are the median, IQR and corresponding 1.5

IQR limits. The goodness-of-fit gets smaller (i.e. better) for fainter meteors. For ICC7, the

median of the goodness-of-fit at -2.0 mag is 3.0' with an IQR of around +/-1.0'. The median

decreases to 1.0' at 6.0 mag. Also the IQR range narrows towards fainter meteors. For bright

meteors, the median and IQR of ICC9 is better by around 1.0'. Median and IQR converge with

the ICC7 values for fainter meteors but the IQR is slightly broader.

As mentioned in Section 3.3.3.(b), bright meteors overexpose the CCD pixels. This leads to

blooming which results in an additional broadening of the meteor on a single video frame.

Another effect may be that bright meteors are more likely to display a wake (Section 3.3.3.

(a)). Due to these effects the photometric center cannot be determined correctly, which leads

to a larger position determination error for brighter meteors.
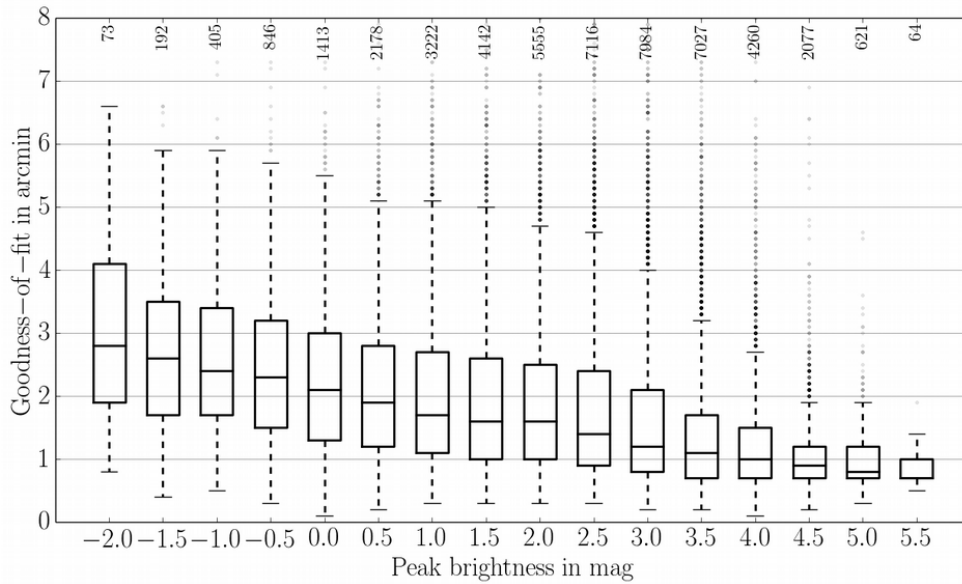
Figure 14 - Goodness-of-fit versus peak brightness in magnitude for ICC7. The box plot shows the median, IQR and 1.5·IQR. The number shown on the top indicates the number of used data points per peak brightness bin.
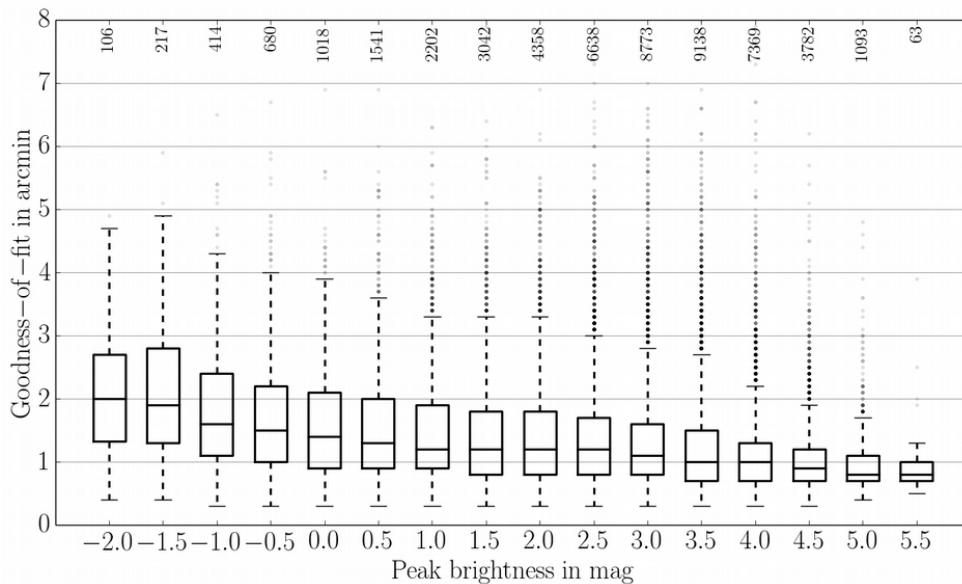
Figure 15 - Goodness-of-fit vs. peak brightness in magnitude for ICC9. The box plot shows the median, IQR and 1.5·IQR. The number shown on the top indicates the number of used data points per peak brightness bin.

1   **5   Discussion**

2   Even though both cameras are identical from a technical point of view, ICC9 detects fainter

3   meteors. We argue in the following that this is a geometrical effect and can be explained by

4   the camera pointing direction.

5   Both camera boresights intersect between Tenerife (ICC7) and La Palma (ICC9) at an altitude

6   of 100 km. Thus, ICC7 is pointing roughly to the West and ICC9 to the East. The elevations

7   of the boresights with respect to the horizon are approximately 53 degrees.

8   In Figure 16 and Figure 17 we plot the angular distance between the camera boresights and

9   the Apex and Antihelion (AH) directions for the time frame 18 UTC to 6 UTC. The red

10   dashed line is the angular distance to the Apex, the blue dashed line to the Antihelion

11   direction. The shaded areas around the lines indicate the annual variation. The black vertical

12   lines indicate the rise times of Antihelion (blue, left line) and Apex (red, right line). Again the

13   shaded area indicates the annual variation. The thick black line is the normalized distribution

14   of the observed meteors as a function of time during the night.
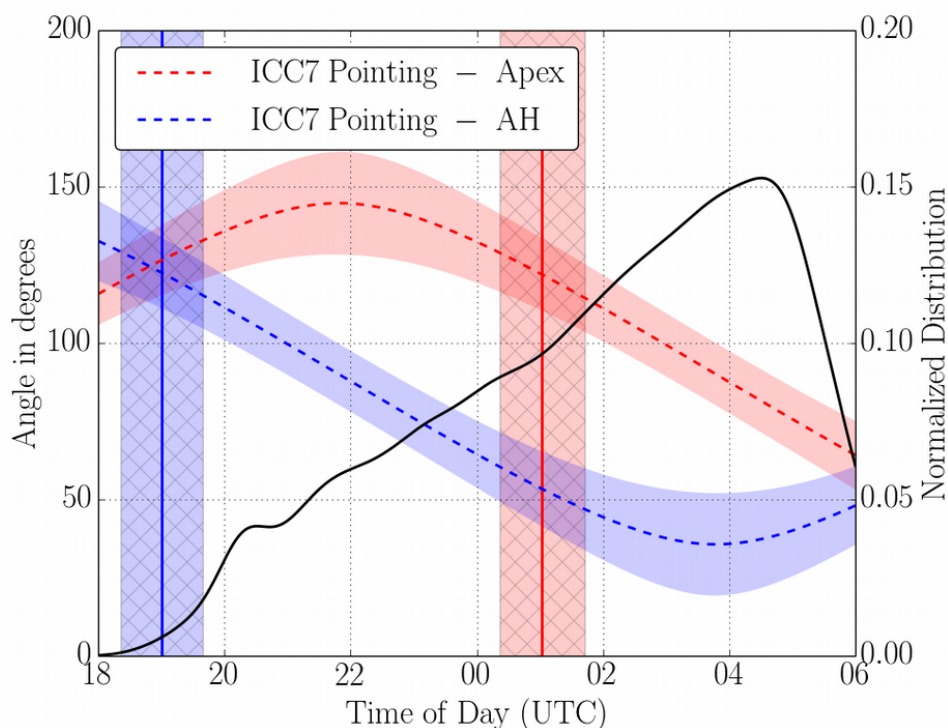
Figure 16 – Angular distance and normalized distribution of detected meteors vs. the time of the day in UTC (ICC7). The red (upper) and blue (lower) dashed curves show the angular distance between the ICC7 boresight and the Apex and Antihelion direction, respectively. The colored areas around the dashed lines show the yearly variations. The solid vertical lines indicate the rising time of the Apex (blue, left) and the Antihelion (red, right) radiants. The hatched area shows the yearly variations. The black curve corresponds to the right axis and gives the normalized number of all detected meteors.
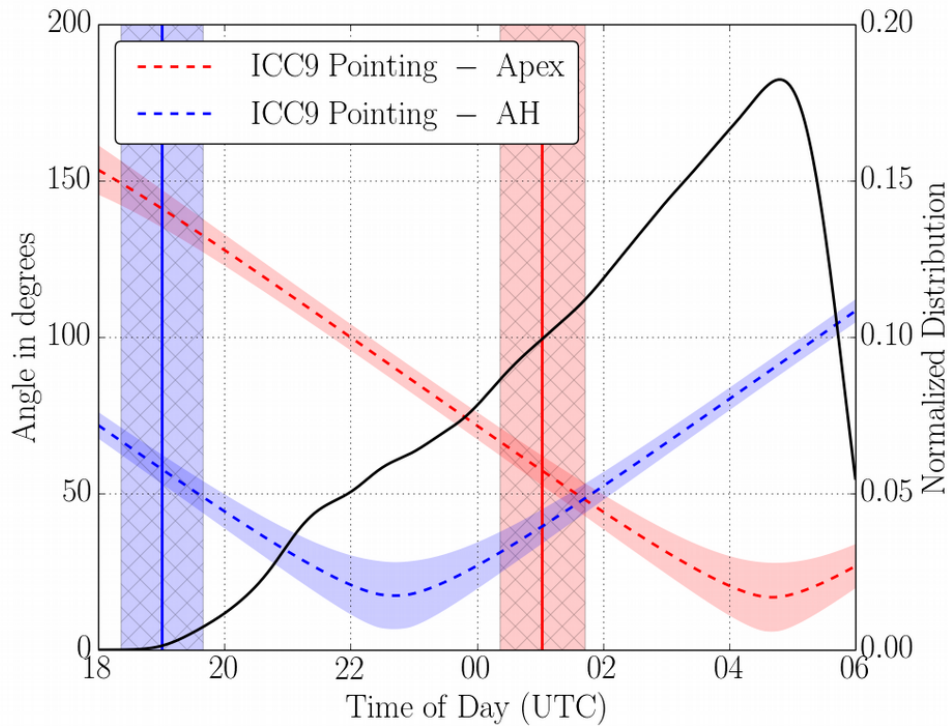
Figure 17 – Angular distance and normalized distribution of detected meteors vs. the time of the day in UTC (ICC9). The red (upper) and blue (lower) dashed curves show the angular distance between the ICC9 boresight and the Apex and Antihelion direction, respectively. The colored area around the dashed lines show the yearly variations. The solid vertical lines indicate the rising time of the Apex (blue, left) and the Antihelion (red, right) radiants. The hatched area shows the yearly variations. The black curve corresponds to the right axis and gives the normalized number of all detected meteors..

The Antihelion direction rises shortly after sunset, the Apex direction after midnight. Since ICC7 is pointing towards the West, its angular distance to the Apex is always much larger than for ICC9.

Figure 18 shows the ratio between the number of meteors for a given apparent velocity of ICC9 to ICC7, using a kernel density estimator (Pedregosa *et al.* 2011). This plot shows an interesting behavior. Starting after midnight, ICC9 sees more meteors than ICC7 in the velocity range of 50 to 200 pxiel/s. The peak moves to higher speeds during the night. After about 04 UTC, ICC9 detects more meteors also for low velocities. We explain this by the distance of the camera boresights to Apex and Antihelion sources. The Apex is very close to

1   the boresight of ICC9 in the morning hours, thus the apparent velocity of these meteors is low.

2   Since the relative speed to the Earth is high, a large number of meteors is visible.
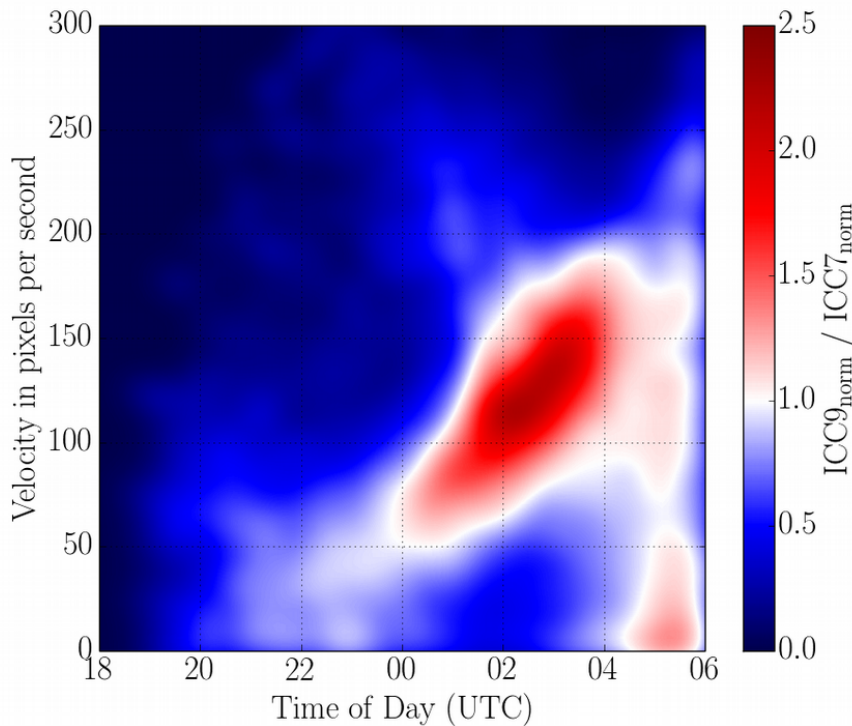
4   **Figure 18 - Ratio plot of the velocity in pixels per second of ICC9 divided by ICC7 vs. the detection time.**

5   **The ratio is color coded and given in the right color bar.**

6   The larger number of slow meteors in ICC9 also explains Figure 19. Since the meteors are

7   slower, they spend more time on a pixel and fainter meteors can be detected. This is an

8   important finding e.g. for determining flux densities. The limiting magnitude determined for

9   stars will be identical for identical systems, no matter where the camera is pointing. However,

10   the detection threshold for meteors will be different.
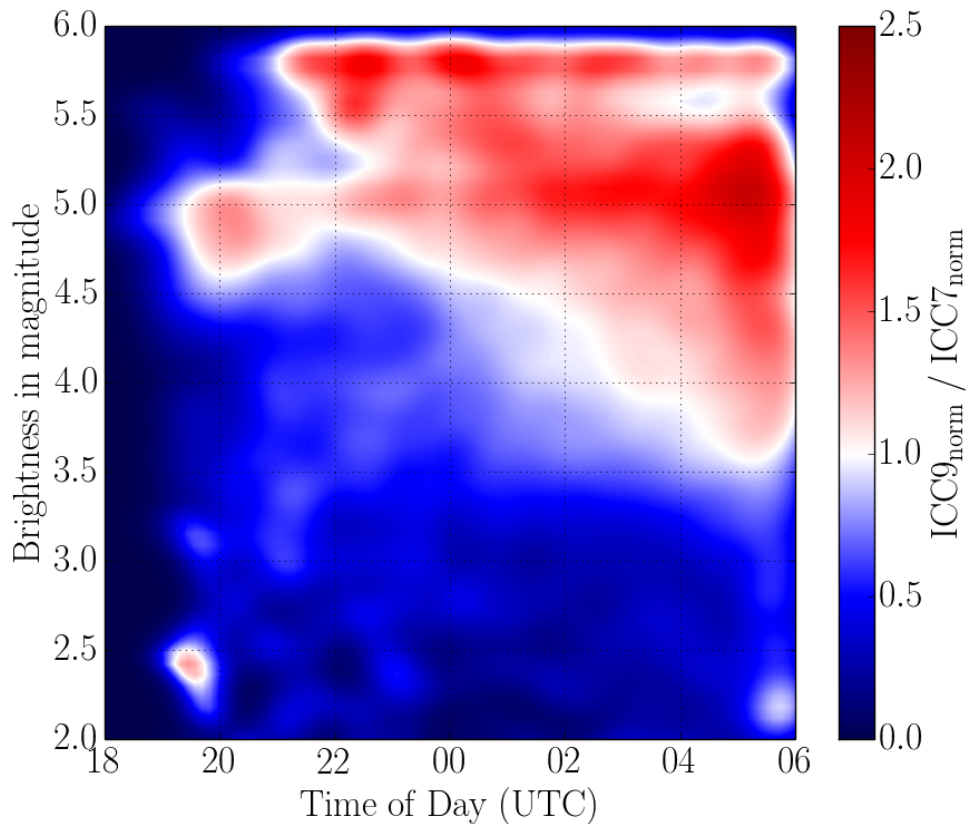
Figure 19 - Ratio plot of the faintest brightness measurements of ICC9 divided by ICC7 vs. the detection

time. The ratio is color coded and given in the right color bar.

In Figure 14 and Figure 15 we showed that the goodness-of-fit is a function of the magnitude.

Since the magnitude distribution changes over the night, also the goodness-of-fit will change

over night. This is illustrated in Figure 20 and Figure 21. The goodness-of-fit is best during

the evening hours, and gets worse towards the morning. The solid line indicates the median

value, the dashed lines the IQRs. The values start at around 0.7' (ICC7) and 1.0' (ICC9) and

decrease over the night. We claim that this is a result of the changing magnitude distribution

over the night.
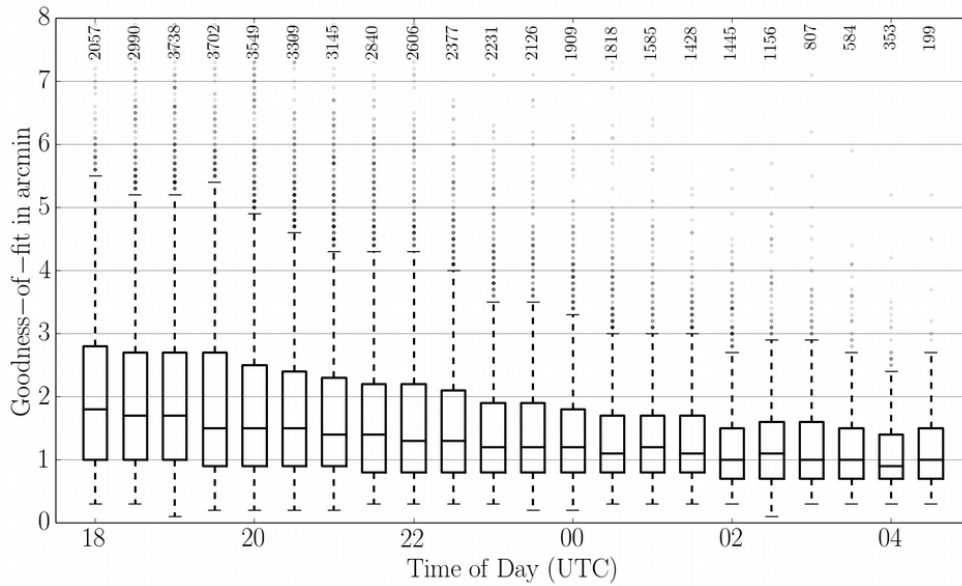
Figure 20 – Goodness-of-fit vs. detection time for ICC7. The box plot shows the median, IQR and 1.5·IQR.

The number shown on the top indicates the number of used data points per peak brightness bin.
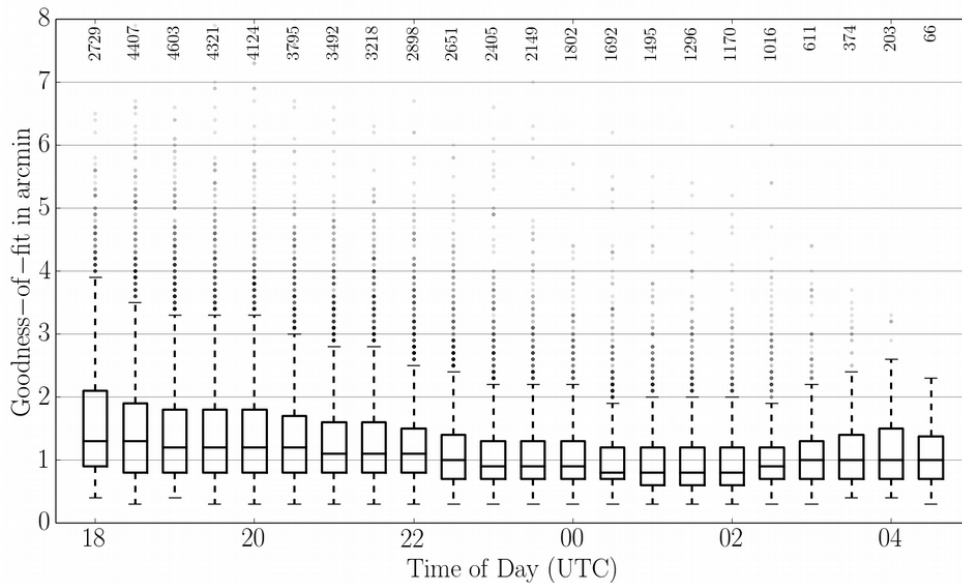
Figure 21 - Goodness-of-fit vs. detection time for ICC9. The box plot shows the median, IQR and 1.5·IQR.

The number shown on the top indicates the number of used data points per peak brightness bin.

1   Figure 22 shows three plots of the normalized length of a meteor in frames versus time for

2   both ICC7 and ICC9, plus the ratio between two distributions. For each frame length bin, the

3   integral of the distribution is 1. The color map limits are the same for both cameras to

4   visualize the differences between both camera systems. It can be seen that both distributions

5   show a similar evolution over time. Longer meteors are dominantly present during the

6   evening and midnight hours and short meteors appear mostly during the morning hours.

7   However, the distributions of ICC7 are wider spread than the distributions of ICC9. The ratio

8   indicates a higher contribution of short meteors for ICC9, by a factor of up to 2. We explain

9   this again by the Apex meteors. ICC9 points closer to the Apex than ICC7, in particular

10   during the morning hours. Thus Apex meteors appear shorter in ICC9.
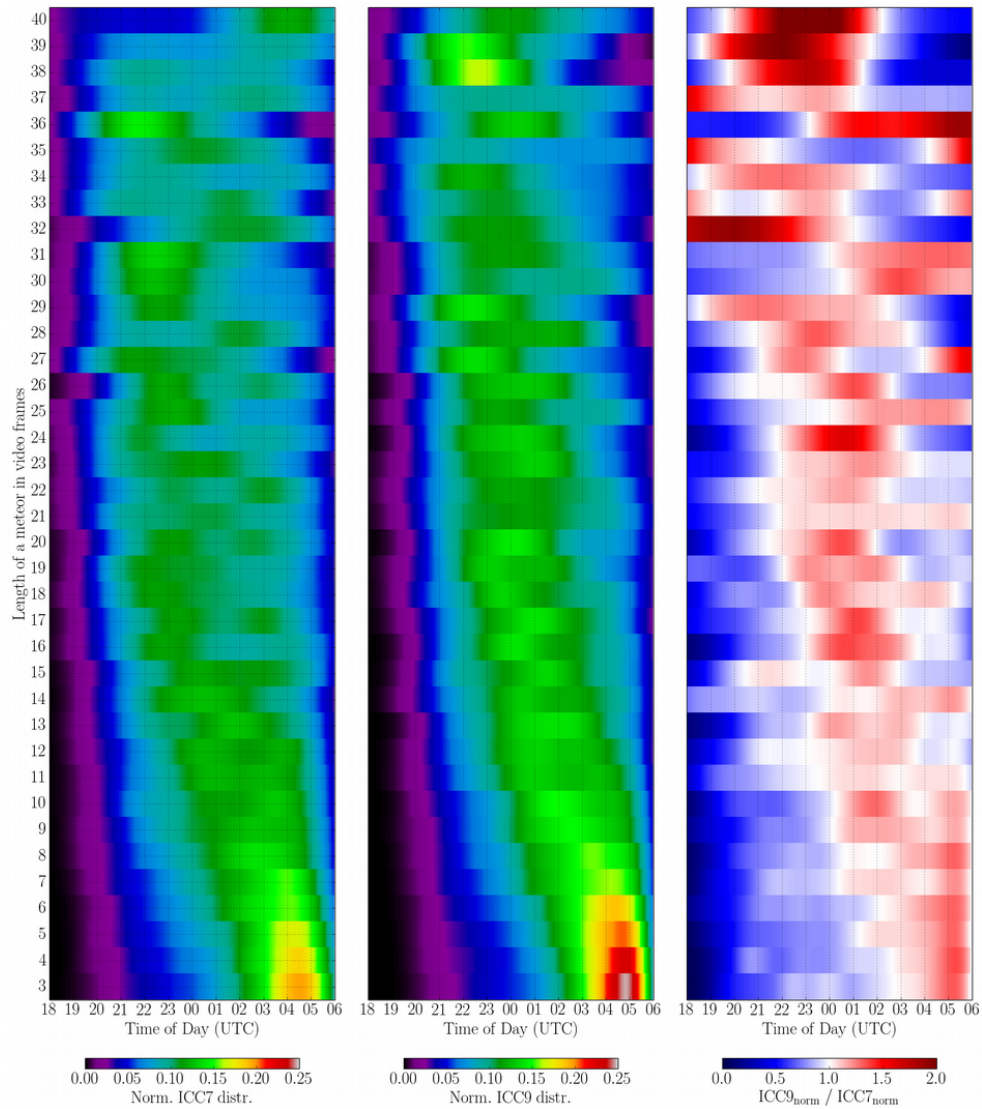
Figure 22 - Ratio plot of the distribution of the normalized length of a meteor in frames of ICC9 divided by ICC7. Each frame distribution is shown vs. the detection time. The ratio is color-coded, with the values given in the bottom color bar.

6   Conclusion

In Section 3.3 we have listed the expected errors and biases coming from the instrument itself, from the measurement pipeline, and from statistical sources. Here we map the findings of the previous section to these errors.

1   Mechanical/thermal stability: Any mechanical/thermal instability would result in a shift of the
2   field of view relative to an Earth-fixed direction. This would shift the measured position of a
3   meteor. When visually inspecting the data, MetRec allows to overlay the expected star
4   positions with the real image. This was done regularly, and such a shift was observed in very
5   rare cases towards the morning hours. It was typically less than 2 pixels. Since it only occured
6   in a few nights, it was not considered in this analysis and would deserve further study.

7   Brightness drop-off: The drop-off of brightness towards the edges of the optical system results
8   in a loss of about 55 %. This will be an important effect when computing flux densities using
9   the limiting magnitude of the system - the detected meteor numbers really are a function of
10   the position in the field of view. The drop-off is larger than what would be expected from pure
11   geometrical effects. It is assumed that this is an effect of the image intensifier. For non-
12   intensified systems we would expect this effect to be less severe.

13   Astrometric accuracy: The measurement accuracy of meteor positions (astrometry) is
14   influenced by a number of the listed errors. Figure 4 shows that the deviation between
15   measured star positions and the expected position as determined by the 3rd-order polynomial
16   plate fit performed by the detection software. It is below 0.2' up to a distance of about 90 % of
17   the diameter of the field of view. When analyzing the goodness-of-fit of individual
18   measurement points relative to the fitted great circle of the meteor's path, errors are larger.
19   Figure 5 and Figure 6 show that typical errors are around 1' to 1.5', depending on the length of
20   the meteor. We assume that these deviations come from the fact that MetRec determines the
21   position of a meteor in a single frame by finding the photometric center of the object. The
22   resulting errors are listed under algorithmic errors in Section 3.3: a possible wake will shift
23   the photometric center to the back; blooming will shift the center in an arbitrary direction;
24   similar for distortion of the meteor image. The possible rescaling from physical pixels to the
25   PAL format (Section 3.3.3 (e)) will also contribute to this result.

26   We conclude that for our camera systems a typical error of 1' to 1.5' should be assumed.

27   The position measurement inaccuracies will also affect the velocity determination. In
28   addition, the first and last frame of the meteor should not be used for velocity determination,
29   for the obvious reason that it is not known at what time during the 40 ms exposure the meteor
30   appears or disappears.

1 We did not do a detailed analysis of random noise affecting the measurements. We assume
2 that since the noise is random it does not produce any bias or shift in any of the
3 measurements, it will only increase the scatter of the data.

4 We find that a major contribution to the detected brightness distribution comes from the
5 pointing direction of the cameras. The pointing direction has to be taken into account when
6 interpreting the detected number of meteors.

7 **7   Literature**

8 Albin, T., Koschny, D., Drolshagen, G., Soja, R., Srama, R., Poppe, B. (2015), Influence of
9 the pointing direction and detector sensitivity variations on the detection rate of a double
10 station meteor camera. In Rault J.-L. and Roggemans P., editors, Proceedings of the
11 International Meteor Conference, Mistelbach, Austria, 27-30 August 2015. IMO, pages 226 –
12 232.

13 Albin, T., Koschny, D., Drolshagen, G., Soja, R., Poppe, B., Srama, R. (2015), Influence of
14 the pointing direction and detector sensitivity variations on the detection rate of a double
15 station meteor camera. In Rault J.-L. and Roggemans P., editors, Proceedings of the
16 International Meteor Conference, Mistelbach, Austria, 27-30 August 2015. IMO, pages 214 –
17 219.

18 Barentsen, G., Koschny, D., The IMO Virtual Meteor Observatory (VMO): Architectural
19 design (2008), Earth, Moon, and Planets, Volume 102, Issue 1-4, pages 247-252.

20 Cooke, W., Moser, D.E. (2012), The status of the NASA All-Sky Fireball network, in:
21 Gyssens, M., Roggemans, P., editors, Proceedings of the International Meteor Conference,
22 Sibiu, Romania, 15-18 September 2011, IMO, pages 9-12.

23 Drolshagen, E., Ott, T., Koschny, D., Drolshagen, G., Poppe, B. (2014), Meteor velocity
24 distribution from CILBO double station video camera dat. In: Rault J.-L., and Roggemans P.,
25 editors, Proceedings of the International Meteor Conference, Giron, France, 18–21 September
26 2014. IMO, pages 16-22.

27 Jenniskens, P. Gural, P.S., Dynneson, L., Grigsby, B.J., Newman, K.E., Borden, M., Koop,
28 M., Holman, D. (2011), CAMS: Cameras for Allsky Meteor Surveillance to establish minbor
29 meteor showers. Icarus Vol. 216, pp. 40-61.

1   Koschny D., Bettonvil F., Licandro J., van der Luijt C., Mc Auliffe J., Smit H., Svendhem H.,

2   de Wit F., Witasse O. and Zender J. (2013). "A double-station meteor camera setup in the

3   Canary Islands - CILBO". Geoscientific Instrumentation Methods and Data Systems, **2**, 339–

4   348.

5   Kretschmer, J., Drolshagen, S., Koschny, D., Drolshagen, G., Poppe, B. (2015), De-biasing

6   CILBO meteor observational data to mass fluxes. In Rault J.-L. and Roggemans P., editors,

7   Proceedings of the International Meteor Conference, Mistelbach, Austria, 27-30 August 2015.

8   IMO, pages 209-213.

9   Molau, S. (1999), The meteor detection software MetRec (1999), in Arlt, R. and Knöfel A.,

10 editors, Proceedings of the International Meteor Conference, Stará Lesná 20-23 August 1998,

11 IMO, pages 9-16.

12 Molau, S. (2014), MetRec - Meteor Recognition Software Version 5.2. Available at

13 http://www.metrec.org/download/readme.txt.

14 Molau, S., Kac, J., Crivello, S., Stomeo, E., Barentsen, G., Goncalves, R., Saraiva, C.,

15 Maciewski, M., Maslov, M. (2015), Results of the IMO Video Meteor Network - April 2015.

16 WGN, Journal of the International Meteor Organization, vol. 43, no. 4, p. 115-120.

17 Ott T., Drolshagen E., Koschny D., Drolshagen G., and Poppe B. (2014). "Meteoroid flux

18 determination using image intensified video camera data from the CILBO double station". In

19 Rault J.-L., and Roggemans P., editors, Proceedings of the International Meteor Conference,

20 Giron, France, 18–21 September 2014. IMO, pages 23-29.

21 Pedregosa, F., Varoquaux, G., Gramfort, A., Michel, V., Thirion, B., Grisel, O., Blondel, M.,

22 Prettenhofer, P., Weiss, R., Dubourg, V., Vanderplas, J., Passos, A., Cournapeau, D., Brucher,

23 M., Perrot, M. and Duchesnay, E. (2011). "Scikit-learn: Machine Learning in Python". Journal

24 of Machine Learning Research, Vol 12, p. 2825-2830.

25 SonotaCo, T., Molau, S., Koschny, D. (2010), Amateur contributions to meteor astronomy,

26 Europea Planetary Science Congress 2010, held 20-24 September in Rome, Italy, p. 798

27 (abstract).

28 Weryk, R. J., Campbell-Brown, M.D., Wiegert, P.A., Brown, P.G., Krzeminski, Z., Musci, R.

29 (2013), The Canadian Automated Meteor Observatory (CAMO): System overview. Icarus,

30 Vol. 225, Iss. 1, p. 614-622.

1   9. Acknowledgements

2   We acknowledge the non-tiring effort of Hans Smit and Cornelis van der Luijt (ESA/Space

3   Science Office) of keeping the cameras operational. CILBO hardware and maintenance are

4   funded thanks to the research faculty of ESA/Space Science Office. We also acknowledge the

5   Instituto de Astrofisica de Canarias (J. Licandro) which hosts the CILBO system and provides

6   local support.